

Testing subhalo abundance matching with galaxy kinematics

Fedir Boreiko^{*,1,2,3}, Tariq Yasin¹, Harry Desmond⁴, Richard Stiskalek¹ and Matt J. Jarvis^{1,5}

¹ Astrophysics, University of Oxford, Denys Wilkinson Building, Keble Road, Oxford, OX1 3RH, UK

² Institute of Astronomy, University of Cambridge, Madingley Road, Cambridge CB3 0HA, UK

³ Department of Physics and Astronomy, University of Manchester, Manchester M13 9PL, UK

⁴ Institute of Cosmology & Gravitation, University of Portsmouth, Dennis Sciama Building, Portsmouth, PO1 3FX, UK

⁵ Department of Physics and Astronomy, University of the Western Cape, Robert Sobukwe Road, 7535 Bellville, Cape Town, South Africa

13 January 2026

ABSTRACT

The rotation velocities of disc galaxies trace dark matter halo structure, providing direct constraints on the galaxy–halo connection. We construct a Bayesian forward model to connect the dark matter halo population predicted by Λ CDM with an observed sample of disc galaxies (SPARC) through their maximum rotation velocities. Our approach combines a subhalo abundance matching scheme (accounting for assembly bias) with a parameterised halo response to galaxy formation. When assuming no correlation between selection in the SPARC survey and halo properties, reproducing the observed velocities requires strong halo expansion, low abundance matching scatter (< 0.15 dex at 1σ) and a halo proxy that strongly suppresses the stellar masses in satellite haloes. This is in clear tension with independent clustering constraints. Allowing for SPARC-like galaxies to preferentially populate low V_{\max} haloes at fixed virial mass greatly improves the goodness-of-fit and resolves these tensions: the preferred halo response shifts to mild contraction, the abundance matching scatter increases to $\sigma_{\text{SHAM}} = 0.19^{+0.13}_{-0.11}$ dex and the proxy becomes consistent with clustering. However, the inferred selection threshold is extreme, implying that SPARC galaxies occupy the lowest ~ 16 per cent of the $V_{\max, \text{halo}}$ distribution at fixed M_{vir} . Moreover, even with selection, the inferred scatter remains in statistical disagreement with the low-mass clustering constraints, which are most representative of the SPARC galaxies in our sample. Our analysis highlights the advantage of augmenting clustering-based constraints on the galaxy–halo connection with kinematics and suggests a possible tension using current data.

Key words: dark matter – galaxies: haloes – galaxies: kinematics and dynamics – galaxies: formation – methods: statistical

1 INTRODUCTION

In Λ CDM, every galaxy resides within a dark matter halo whose properties—mass, concentration, formation history—shape the galaxy’s observable characteristics. Constraining this “galaxy–halo connection” empirically is essential both for building theoretical models of galaxy formation and for using observed galaxy populations to infer the underlying dark matter distribution (Wechsler & Tinker 2018). A particularly direct probe comes from galaxy kinematics: the internal motions of stars and gas trace the total gravitational potential, and hence the dark matter content, of individual systems.

Rotation curves—the circular velocity of disc galaxies as a function of galactocentric radius—provide detailed constraints on the radial mass distribution. H_I observations revealed that rotation curves remain flat or rising well beyond the optical disc (Rubin & Ford 1970; Bosma 1981), implying mass profiles that extend far beyond the visible baryons. This established dark matter haloes as a ubiquitous component of disc galaxies (Sofue & Rubin 2001). In recent years,

the SPARC database (Lelli et al. 2016) has provided high-quality rotation curves for 175 nearby galaxies, combining H_I interferometry with Spitzer 3.6 μm photometry (Werner et al. 2004) to enable precise decomposition into baryonic and dark matter contributions.

Rotation curves are often summarised by characteristic velocity statistics such as the peak velocity V_{\max} , the asymptotic flat velocity V_{flat} , or the velocity at a fixed multiple of the disc scale length $V_{2.2}$ (Ponomareva et al. 2017, 2018; Lelli et al. 2019). These summary statistics correlate tightly with baryonic mass: the Baryonic Tully–Fisher Relation (BTFR) connects a galaxy’s total baryonic mass to its rotational velocity with remarkably small scatter (~ 0.1 dex; Tully & Fisher 1977; McGaugh et al. 2000; Lelli et al. 2019; Desmond 2017). This tightness places strong constraints on the galaxy–halo connection and has been used extensively to test dark matter models and galaxy formation physics (Trujillo-Gomez et al. 2011; Desmond & Wechsler 2015; Desmond et al. 2019; Ferrero et al. 2017).

Several studies have used subhalo abundance matching (SHAM) to forward-model galaxy scaling relations such as the BTFR (Trujillo-Gomez et al. 2011; Desmond & Wechsler

* Email: fedir.boreiko@gmail.com

2015; Ferrero et al. 2017). SHAM provides a framework for connecting galaxies to haloes in dark-matter-only simulations by rank-ordering both populations—typically by luminosity or stellar mass, and a halo property such as present-day virial mass M_{vir} or the peak mass across a halo’s history M_{peak} —and matching them with some scatter (Conroy et al. 2006; Behroozi et al. 2010; Moster et al. 2010). The intrinsic scatter σ_{SHAM} (typically ~ 0.2 dex; Reddick et al. 2013; Desmond & Wechsler 2015) is routinely constrained using galaxy clustering. SHAM successfully reproduces galaxy clustering, satellite fractions, and other statistics, providing strong constraints on the stellar-to-halo mass relation (Reddick et al. 2013).

Modern abundance matching employs multi-property halo proxies to account for assembly bias—correlations between clustering and secondary halo properties at fixed mass—that can bias inferences if ignored (Hearin & Watson 2013; Zentner et al. 2014; Mao et al. 2017). Lehmann et al. (2016) introduced a proxy that smoothly interpolates between peak halo mass M_{peak} and peak maximum circular velocity $V_{\text{max,peak}}$, controlling sensitivity to halo concentration at fixed mass. The interpolation is controlled by a single free parameter, which they constrained along with the scatter using clustering data (their best-fit values were subsequently tested against kinematics by Desmond 2017). This accommodates assembly bias within the SHAM framework.

In this work, we improve on previous SHAM-based models of galaxy kinematics in two ways. First, rather than using a fixed SHAM proxy, we adopt the compound proxy of Stiskalek et al. (2021, hereafter S21), which interpolates between M_{vir} and M_{peak} , and allow its parameter α to be constrained along with the SHAM scatter in the inference. This affords a test of whether the galaxy–halo connection inferred from clustering is consistent with that inferred from galaxy dynamics. Second, unlike previous works that fit population-level summary statistics such as the BTFR slope, scatter and intercept (Trujillo-Gomez et al. 2011; Desmond & Wechsler 2015; Ferrero et al. 2017; Desmond 2017), we construct a full likelihood for the observed maximum circular velocity V_{max} of *each individual galaxy* in SPARC, maximising the information extracted from the galaxy–halo connection without compression into the summary statistics of the TFR properties.

We use V_{max} as our kinematic observable for two reasons. First, although V_{flat} is the quantity that correlates best with baryonic properties (Lelli et al. 2019), it is more difficult to measure than V_{max} , requiring data at higher galactocentric radius as well as a subjective definition of what constitutes “flatness”. Second, V_{max} is close in information content to the $\text{H}\alpha$ line width W_{50} (Yasin et al. 2023a), a velocity summary statistic that will be available for millions of galaxies at cosmological redshifts from current and upcoming $\text{H}\alpha$ surveys such as MIGHTEE (Jarvis et al. 2016; Ponomareva et al. 2021; Vărăsteau et al. 2025), WALLABY (Koribalski & et al. 2020), LADUMA (Blyth et al. 2016), DINGO (Rhee et al. 2023) and eventually, the SKA (Blyth et al. 2015). Developing and validating forward models using V_{max} therefore enables application to much larger samples at higher redshift.

Alongside the SHAM parameters, we consider free parameters governing the response of the dark matter halo to galaxy formation (spanning contraction to expansion) and a “selection parameter” allowing SPARC galaxies to occupy a biased subset of the halo population. Specifically, we ask:

- What values of the SHAM parameters (α , σ_{SHAM}) are preferred by SPARC kinematics, and are these consistent with clustering constraints?
- Is halo expansion or contraction required to match the observed velocities?
- To what extent is selection important for modelling the kinematics, and how does this impact the consistency with inferences from clustering?
- What do these results imply for the host haloes of gas-rich, late-type galaxies?

The paper is structured as follows. Section 2 describes the observational and simulation data we use. Section 3 details our forward-modelling methodology: SHAM, rotation curve calculation including halo response, selection modelling and the likelihood framework. Section 4 presents results from mock validation and fits to the real data. We discuss implications and compare to the literature in Section 5, and conclude in Section 6. We denote base-10 logarithms as \log and natural logarithms as \ln .

2 OBSERVED AND SIMULATED DATA

2.1 SPARC

Our kinematic data are derived from the SPARC database¹ (Lelli et al. 2016). This contains 175 late-type galaxies for which both spatially-resolved $\text{H}\alpha$ and $\text{H}\alpha$ rotation curves and near-infrared Spitzer photometry are available, providing a detailed view of the distribution of stars and gas.

The sample covers a wide range of luminosities (from 10^7 to $10^{12} L_{\odot}$), surface brightness (~ 5 to $5000 L_{\odot} \text{pc}^{-2}$), gas mass (from 10^7 to $10^{10.6} M_{\odot}$), and morphology (from S0 to Im/BCD types). At $3.6 \mu\text{m}$, the mass-to-light ratio is assumed to remain relatively stable (McGaugh & Schombert 2014), aiding in disentangling the velocity contributions of stellar mass and dark matter (but see Vărăsteau et al. 2025 for evidence that this may not be universally true).

Within our likelihood framework, we compare predicted V_{max} values with those measured from SPARC rotation curves to infer model parameters. This comparison is based on a sub-sample of 153 galaxies used in SPARC BTFR analyses, where galaxies with low inclinations and low-quality rotation curves have been excluded (Lelli et al. 2019). We adopt the SPARC observational uncertainties on V_{max} , $\sigma_{V_{\text{max}}}^{(\text{SPARC})}$, which arise from rotation curve measurements and disc inclination; the latter typically dominates (Lelli et al. 2019). We treat these as Gaussian and uncorrelated between galaxies.

2.2 NASA-Sloan Atlas

We obtain the observed stellar mass function (SMF) from the NASA-Sloan Atlas² (NSA), a catalogue of nearby galaxies combining the Sloan Digital Sky Survey (SDSS) with the Galaxy Evolution Explorer (Martin et al. 2005). We use NSA v1_0_1, based on SDSS DR13 (Albareti et al. 2017), which

¹ <https://astroweb.case.edu/SPARC/>

² <https://www.sdss4.org/dr17/manga/manga-target-selection/nsa/>

contains $\sim 640,000$ galaxies out to redshift $z = 0.15$. The catalogue includes both elliptical Petrosian and Sérsic aperture photometry, K-corrected to $z = 0.0$, with the former considered more reliable. We therefore adopt the elliptical Petrosian SMF following S21, computed using the $1/V_{\text{max,vol}}$ method (Schmidt 1968). This corrects for Malmquist bias by weighting each galaxy by the inverse of the maximum comoving volume within which it is detectable.

Our abundance matching uses the NSA SMF, yet only 91 SPARC galaxies have NSA stellar masses. For these, the NSA M_* estimates are statistically consistent with SPARC values assuming ~ 0.2 dex uncertainties on NSA values (Yasin et al. 2023b). This consistency justifies using SPARC stellar masses for individual galaxies while employing the NSA-derived SMF for the input to SHAM.

2.3 Simulation Data

We use the $140 h^{-1}$ Mpc ‘‘Shin-Uchuu’’ box from the Uchuu suite of cosmological N -body simulations (Ishiyama et al. 2021), run with the GreeM N -body code (Ishiyama et al. 2009, 2012). The simulation includes 6400^3 particles, each with a mass of $8.97 \times 10^5 h^{-1} M_\odot$ and a force softening length of $0.4 h^{-1}$ kpc, and adopts the 2018 *Planck* flat Λ CDM cosmology (Planck Collaboration et al. 2020): $H_0 = 67.74 \text{ km s}^{-1} \text{ Mpc}^{-1}$, $\Omega_m = 0.3089$, $\Omega_\Lambda = 0.6911$, $n_s = 0.9667$, and $\sigma_8 = 0.8159$. Haloes and satellite haloes are identified with the `Rockstar` halo finder (Behroozi et al. 2012a), with merger trees constructed using `Consistent Trees` (Behroozi et al. 2012b). Halo masses are defined by the virial overdensity $\Delta_{\text{vir}} = 178$ (Bryan & Norman 1998). Our sample includes haloes with $M_{\text{vir}} > 10^{10} M_\odot$.

3 METHODS

We summarise our method for modelling galaxy rotation curves below; each step is detailed in the subsequent sections.

- (i) Apply SHAM to assign stellar masses to haloes using a generalised proxy parametrised by α and intrinsic scatter σ_{SHAM} (Section 3.1.1).
- (ii) Optionally, select haloes by their maximum circular velocity $V_{\text{max,halo}}$ to model how selection effects influence α , since SPARC may be a biased sample of the halo population (Section 3.1.4).
- (iii) Generate Monte Carlo realisations of galaxy stellar masses by sampling their observational uncertainties, and associate them with haloes via SHAM. (Section 3.1.2).
- (iv) Modify halo density profiles to account for disc formation—ranging from adiabatic contraction to expansion—then compute rotation curves and extract V_{max} (Section 3.1.3).
- (v) Repeat the above steps by resampling the SHAM galaxy–halo connection varying the noise realisation at fixed σ_{SHAM} to capture stochasticity in the stellar–halo mass relation, collecting V_{max} samples across realisations.
- (vi) Compare each galaxy’s V_{max} distribution with observations to evaluate the likelihood; the total likelihood is then the product over all galaxies (Section 3.2).
- (vii) Evaluate the likelihood on a grid of model parameters.
- (viii) Interpolate the likelihood grid and sample posterior

distributions of the model parameters using Markov Chain Monte Carlo (MCMC).

3.1 Modelling V_{max}

3.1.1 Subhalo abundance matching

SHAM is an empirical framework that associates galaxies with dark matter haloes by assuming a monotonic relation between (e.g.) stellar mass and a halo property (the ‘‘halo proxy’’). Haloes are rank-ordered by the chosen proxy, while galaxies are rank-ordered by stellar mass using an observed SMF (here from the NSA). Galaxies and haloes are then matched by rank: the galaxy with the n^{th} largest stellar mass is assigned to the halo with the n^{th} largest proxy value (Kravtsov et al. 2004a; Vale & Ostriker 2004; Conroy et al. 2006; Behroozi et al. 2010; Moster et al. 2010). SHAM reproduces observed galaxy clustering, galaxy–galaxy lensing, group catalogues, and void statistics (Conroy et al. 2006; Vale & Ostriker 2006; Moster et al. 2010; Reddick et al. 2013), as well as stellar–halo mass relations inferred from weak lensing and satellite kinematics (Behroozi et al. 2010).

SHAM can incorporate non-zero scatter σ_{SHAM} , the standard deviation of stellar mass at fixed halo proxy (Tasitsiomi et al. 2004; Behroozi et al. 2010). This scatter largely reflects the influence of secondary halo properties on baryonic content, particularly accretion history (Tinker et al. 2017). We treat σ_{SHAM} as a free parameter and implement scatter using the deconvolution method of Behroozi et al. (2010): galaxies are first matched at zero scatter, stellar masses are perturbed along the galaxy–halo ladder, and abundances are adjusted to restore consistency with the input SMF at chosen σ_{SHAM} .

We adopt the generalised halo proxy m_α from S21, who found it to perform significantly better than the Lehmann et al. (2016) proxy for faint optically selected samples, while performing equally well for bright samples. This proxy interpolates between peak virial mass M_{peak} and present-day virial mass M_{vir} ,

$$m_\alpha = M_{\text{vir}} \left(\frac{M_{\text{peak}}}{M_{\text{vir}}} \right)^\alpha, \quad (1)$$

where α is a free parameter. For $\alpha = 0$, haloes are ranked by M_{vir} and for $\alpha = 1$ by M_{peak} , with larger α boosting the clustering signal. Varying α controls the ranking of haloes that have lost mass (typically satellites): $\alpha > 0$ up-ranks haloes whose mass peaked in the past, while $\alpha < 0$ down-ranks them.

3.1.2 Forward modelling the BTFR

We generate N_{stellar} Monte Carlo samples for each SPARC galaxy to estimate stellar and gas masses from the photometric data. First, we draw N_{stellar} samples of distance, $L_{[3.6]}$, and M_{HI} from Gaussian distributions centred on the SPARC values with standard deviations set by measurement uncertainties. Adopting mass-to-light ratios $\Upsilon_* = 0.5 M_\odot/L_\odot$ (disc) and $\Upsilon_* = 0.7 M_\odot/L_\odot$ (bulge), each with 0.1 dex uncertainty (Lelli et al. 2016), we sample Υ_* similarly. Stellar and gas masses are computed as

$$\begin{aligned} M_* &= (L_{[3.6]} - L_{\text{bulge}})\Upsilon_{\text{disc}} + L_{\text{bulge}}\Upsilon_{\text{bulge}}, \\ M_{\text{gas}} &= 1.33 M_{\text{HI}}, \end{aligned} \quad (2)$$

where L_{bulge} is the bulge luminosity from photometric decomposition³. We rescale masses to the sampled distance, as SPARC tabulates luminosities/masses assuming the fiducial distances to each galaxy. This yields N_{stellar} samples of M_{\star} and M_{gas} for each galaxy.

We assign each M_{\star} sample to a halo by matching to the nearest stellar mass in the SHAM catalogue, yielding N_{stellar} galaxy–halo pairs per galaxy. This propagates M_{\star} uncertainties into the halo assignment and incorporates SHAM scatter, so that the pairing reflects both observational uncertainties and intrinsic scatter in the galaxy–halo connection.

The total circular velocity is the quadrature sum of contributions from dark matter, stellar bulge, stellar disc, and gas disc,

$$V_C^2 = V_{\text{dm}}|V_{\text{dm}}| + V_{\text{disc}}|V_{\text{disc}}| + V_{\text{bulge}}|V_{\text{bulge}}| + V_{\text{gas}}|V_{\text{gas}}|, \quad (3)$$

where V_{disc} and V_{bulge} are scaled from the fiducial SPARC stellar velocity contributions (computed assuming $\Upsilon = 1 M_{\odot}/L_{\odot}$ (Lelli et al. 2016)) according to the sampled mass-to-light ratios:

$$\begin{aligned} V_{\text{disc}} &= \sqrt{\Upsilon_{\text{disc}}} V_{\text{disc, fid}} \\ V_{\text{bulge}} &= \sqrt{\Upsilon_{\text{bulge}}} V_{\text{bulge, fid}} \end{aligned} \quad (4)$$

For the dark matter contribution, we assume the Navarro–Frenk–White profile (NFW; Navarro et al. 1997)

$$\rho_{\text{NFW}}(r) = \frac{\rho_s}{(r/r_s)[1 + (r/r_s)]^2}, \quad (5)$$

where r_s is the scale radius and ρ_s the characteristic density. The enclosed mass within radius r is

$$M_{\text{NFW}}(r) = 4\pi\rho_s r_s^3 \left[\ln(1 + x) - \frac{x}{1 + x} \right], \quad (6)$$

where $x = r/r_s$. The circular velocity contribution from dark matter is

$$V_{\text{dm}}(r) = \sqrt{\frac{GM_{\text{NFW}}(r)}{r}}. \quad (7)$$

From each rotation curve we extract V_{max} , defined as the peak circular velocity, and compute $M_{\text{bar}} = M_{\star} + M_{\text{gas}}$. For a given SHAM realisation, this yields N_{stellar} samples of $(V_{\text{max}}, M_{\text{bar}})$ per galaxy. We repeat the procedure for N_{SHAM} SHAM realisations at fixed $(\alpha, \sigma_{\text{SHAM}})$, resampling the noise each time to capture stochasticity in the galaxy–halo connection.

Collecting all $N_{\text{stellar}} \times N_{\text{SHAM}}$ samples per galaxy, we transform V_{max} and M_{bar} to log. Figure 1 shows the predicted BTFR for illustrative parameters and compares it to the SPARC data.

3.1.3 Halo response

Dark matter haloes in N -body simulations agree well with the NFW profile, but galaxy evolution modifies this structure. The classic expectation is adiabatic contraction: as baryons cool and collapse into a central disc, they deepen the potential

³ More realistically, L_{bulge} should scale with $L_{[3.6]}$, but as the luminosity uncertainties are small compared to other uncertainties, especially the mass-to-light ratios, this does not make an appreciable difference.

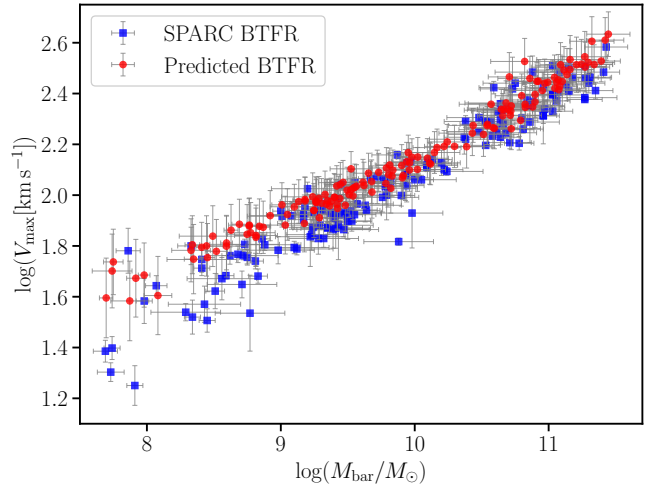


Figure 1. Comparison of forward-modelled (red) and observed SPARC (blue) BTFRs. Model parameters are $\tan^{-1} \alpha = 0.5$, $\sigma_{\text{SHAM}} = 0.1$ dex, $\nu = -1.1$, with no halo selection ($x = 0$).

and draw in surrounding dark matter, steepening the inner profile (Blumenthal et al. 1986; Kravtsov et al. 2004b; Gnedin et al. 2011). However, bursty star formation and feedback-driven outflows can transfer energy to the dark matter and cause the opposite effect—halo expansion and core formation (Pontzen & Governato 2012). The net response depends on the balance between these processes, which varies with halo mass and star formation efficiency: cores form most readily at intermediate stellar-to-halo mass ratios where feedback is energetic relative to the binding energy, while contraction dominates in more massive systems where baryons deepen the potential faster than feedback can unbind material (Di Cintio et al. 2014; Tollet et al. 2016). Recent work calibrating quasi-adiabatic relaxation models against IllustrisTNG (Pillepich et al. 2018) and EAGLE (Schaye et al. 2015) suggests that the response may additionally depend on halo-centric distance (Velmani & Paranjape 2023), though this is sensitive to the subgrid physics adopted in those simulations.

Given these uncertainties, we adopt a simple parameterisation that spans the full range from contraction to expansion. We use the modified adiabatic contraction framework of Gnedin et al. (2011), which accounts for the eccentricity of dark matter particle orbits, but introduce a parameter ν that continuously interpolates between contraction ($\nu > 0$) and expansion ($\nu < 0$) (Dutton et al. 2007; Desmond & Wechsler 2015).

In this model, we assume that before disc formation, both dark matter and baryons follow the NFW density profile exactly, with baryons initially tracing the dark matter distribution. Upon disc formation, baryons are redistributed into a thin exponential disc. Assuming the halo is spherically symmetric and composed of non-crossing shells, angular momentum is conserved,

$$[M_{\text{dm},i}(\bar{r}_i) + M_{\text{b},i}(\bar{r}_i)]r_i = [M_{\text{dm},f}(\bar{r}_f) + M_{\text{b},f}(\bar{r}_f)]r_f, \quad (8)$$

where subscripts i and f refer to the states before and after disc formation, respectively, and the masses are enclosed within the orbit-averaged radius \bar{r} . Here we use conservation of dark matter mass within a Lagrangian shell, $M_{\text{dm},f}(\bar{r}_f) = M_{\text{dm},i}(\bar{r}_i)$. The equation for \bar{r} is approximated

by a power law

$$\bar{r} = A_0 r_0 \left(\frac{r}{r_0} \right)^w, \quad (9)$$

with $A_0 = 1.6$, $w = 0.8$, and $r_0 = 0.03r_{\text{vir}}$ (Gnedin et al. 2011, eq. 4), where we take the virial radius of the system to equal the halo virial radius, r_{vir} .

Using the baryon fraction $f_b = M_b/(M_{\text{vir}} + M_b)$, we rewrite the initial total enclosed mass as $M_{\text{tot},i}(r) = M_{\text{dm},i}(r)/(1 - f_b)$. Expressing radii in units of r_{vir} as $y \equiv r/r_{\text{vir}}$, we introduce the baryonic mass fraction,

$$m_b(y) = \frac{M_b(r)}{M_{\text{tot}}(r_{\text{vir}})} = f_b \frac{M_b(y)}{M_b(1)}, \quad (10)$$

and the dark matter mass fraction,

$$m_{\text{dm}}(y) = \frac{M_{\text{dm}}(r)}{M_{\text{tot}}(r_{\text{vir}})} = (1 - f_b) \frac{M_{\text{dm}}(y)}{M_{\text{dm}}(1)}. \quad (11)$$

For an initial NFW dark matter distribution,

$$M_{\text{dm}}(y) = \ln(1 + cy) - \frac{cy}{1 + cy}, \quad (12)$$

where c is the halo concentration. For baryons redistributed into an exponential disc,

$$M_b(y) = 1 - \left(1 + \frac{y}{y_b} \right) \exp \left(-\frac{y}{y_b} \right), \quad (13)$$

where $y_b = r_b/r_{\text{vir}}$ is the baryon scalelength in units of r_{vir} . For simplicity, we assume all baryons follow this profile after disc formation, setting $r_b = R_{\text{eff}}/1.67835$, where R_{eff} is the observed effective radius. A more rigorous treatment would separate the disc component and define r_b as its scalelength, requiring an additional model parameter. Finally, using Equations (10) and (11), we rewrite Equation (8) as

$$[m_{\text{dm},i}(\bar{y}_i) + m_{\text{b},f}(\bar{y}_f)] y_f - \frac{m_{\text{dm},i}(\bar{y}_i)}{1 - f_b} y_i = 0, \quad (14)$$

which can be solved iteratively for r_f given halo mass, concentration, virial radius, baryon fraction, and scalelength.

This yields the standard adiabatic contraction solution. To allow for expansion as well as contraction, we adopt the generalised form of Dutton et al. (2007), defining

$$\Gamma(r_i) \equiv \frac{r_f}{r_i}, \quad (15)$$

and setting the true final radius as

$$r_{\text{f,true}} = \Gamma^\nu r_i. \quad (16)$$

The free parameter ν interpolates between standard adiabatic contraction ($\nu = 1$), no halo response ($\nu = 0$), and expansion by the same factor as standard contraction ($\nu = -1$). Given an observed radius $r_{\text{f,true}}$, we iteratively solve for the initial radius r_i and compute the enclosed dark matter mass $M_{\text{dm}}(r_i)$ to evaluate V_{dm} . To reduce computational cost, we precompute a grid over $(c, f_b, r_b, r_{\text{f,true}})$ for each value of ν , storing $M_{\text{dm}}(r_{\text{f,true}})$. During the analysis, we perform multivariate linear interpolation over these grids using `jax.scipy.ndimage` to obtain V_{dm} .

To quantify the accuracy of this interpolation scheme, we validated the precomputed grids against exact calculations. For 20 values of ν spanning the prior range $[-3, 3]$,

we generated 1000 random test points within the parameter space (c, f_b, r_b, r_f) and solved the halo response equations iteratively to determine the true enclosed dark matter mass. Across the majority of the parameter space ($\nu > -2$, $\log c \in [1.0, 3.0]$, $\log f_b \in [-2.5, -1.0]$, $\log r_b \in [-2.5, -1.5]$, $\log r_f \in [-4, 0]$), the interpolation is exceptionally accurate, with a mean percentage error on the enclosed dark matter mass fraction $m_{\text{dm}}(r_f)$ of $\lesssim 0.5$ per cent. Non-negligible deviations (~ 1 – 2 per cent) only occur at the lower limit of halo expansion ($\nu \rightarrow -3.0$). We attribute this slight degradation to the complex behaviour of the density profile under strong feedback, where the mapping between initial and final radii becomes highly non-linear. However, given that these errors remain small and that the extreme ν regime is disfavoured by the data, numerical uncertainties in our posteriors associated with the interpolation are negligible.

3.1.4 Selection model

Since the SPARC sample consists of late-type galaxies, these may occupy a biased subset of haloes with distinct structural and formation characteristics compared to the overall halo population. To account for this, we adopt a simple phenomenological halo selection method based on the present-day maximum circular velocity, $V_{\text{max,halo}}$. The choice of $V_{\text{max,halo}}$ as the selection criterion is motivated by its strong correlation with our observable, the galaxy rotation curve maximum. Since $V_{\text{max,halo}}$ encapsulates both halo mass and concentration, it correlates more strongly with galaxy stellar mass than virial mass alone. Furthermore, haloes with high $V_{\text{max,halo}}$ at fixed virial mass tend to have distinct formation histories, such as earlier formation times or higher concentrations, which correlate with enhanced clustering, i.e. assembly bias (Lehmann et al. 2016).

We consider the halo distribution in $\log V_{\text{max,halo}} - \log M_{\text{vir}}$ space by defining a moving window along the $\log M_{\text{vir}}$ axis with a width of 0.1 dex. Within each window, we determine the threshold $\log V_{\text{max,halo}}$ value above which a fraction x of the haloes reside. By sliding this window in steps of 0.01 dex along the $\log M_{\text{vir}}$ axis, we obtain the x -percentile of $\log V_{\text{max,halo}}$ as a function of $\log M_{\text{vir}}$. We then fit a linear model to these percentile points, yielding a continuous linear threshold. We select haloes by removing all that lie above this threshold for a given $x \in [0, 1]$. Figure 2 illustrates this selection for $x = 0.5$, and Figure 3 shows its effect on the predicted V_{max} distribution.

3.2 Likelihood framework

We obtain the posterior distribution of the model parameters via Bayes' theorem,

$$\mathcal{P}(\boldsymbol{\theta} | \mathcal{D}) = \frac{\mathcal{L}(\mathcal{D} | \boldsymbol{\theta})\pi(\boldsymbol{\theta})}{\mathcal{Z}}, \quad (17)$$

where \mathcal{D} denotes the data, $\boldsymbol{\theta}$ the model parameters, \mathcal{L} the likelihood, π the prior, and \mathcal{Z} the Bayesian evidence,

$$\mathcal{Z} \equiv \int \mathcal{L}(\mathcal{D} | \boldsymbol{\theta})\pi(\boldsymbol{\theta}) d\boldsymbol{\theta}, \quad (18)$$

i.e. the probability of \mathcal{D} under the chosen model. The Bayes factor (evidence ratio) gives the relative probability of two

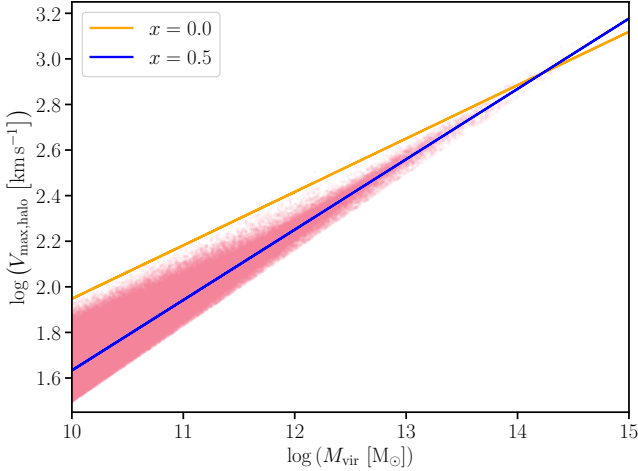


Figure 2. Illustration of the halo-level selection on $V_{\max,\text{halo}}$ at fixed M_{vir} . The solid lines mark the $x = 0$ (orange) and $x = 0.5$ (blue) thresholds, corresponding to the median $V_{\max,\text{halo}}$ at each virial mass. Haloes above this line (higher $V_{\max,\text{halo}}$ at fixed mass) would be excluded.

models given the same data, with qualitative strength often reported on the Jeffreys scale (Jeffreys 1939).

We perform inference on individual V_{\max} values, denoting $v = \log V_{\max}$. For the i^{th} galaxy, we have the measured SPARC log-velocity \mathcal{D}_i with uncertainty σ_i , and N predicted values $\{v_i^{(j)}\}_{j=1}^N$. For a single predicted value $v_i^{(j)}$, the conditional likelihood of observing \mathcal{D}_i is given by a Gaussian likelihood,

$$\mathcal{L}(\mathcal{D}_i \mid v_i^{(j)}, \boldsymbol{\theta}) = \frac{1}{\sqrt{2\pi}\sigma_i} \exp \left[-\frac{1}{2} \left(\frac{\mathcal{D}_i - v_i^{(j)}}{\sigma_i} \right)^2 \right]. \quad (19)$$

In the case of a continuous distribution of $v_i^{(j)}$, the marginal likelihood would be

$$\mathcal{L}(\mathcal{D}_i \mid \boldsymbol{\theta}) = \int \mathcal{L}(\mathcal{D}_i \mid v_i, \boldsymbol{\theta}) p(v_i) dv_i, \quad (20)$$

where $p(v_i) \equiv p(v_i \mid \boldsymbol{\theta})$ is the distribution of the velocity conditioned on the model parameters, implicitly defined by the forward model. We treat it instead as a sum over the Monte Carlo samples:

$$\mathcal{L}(\mathcal{D}_i \mid \boldsymbol{\theta}) \approx \frac{1}{N} \sum_{j=1}^N \mathcal{L}(\mathcal{D}_i \mid v_i^{(j)}, \boldsymbol{\theta}). \quad (21)$$

Figure 3 illustrates this for an example galaxy. The overall log-likelihood is the sum of the log marginal likelihoods over all galaxies,

$$\ln \mathcal{L}(\mathcal{D} \mid \boldsymbol{\theta}) = \sum_i^n \ln \mathcal{L}(\mathcal{D}_i \mid \boldsymbol{\theta}). \quad (22)$$

We evaluate the log-likelihood on a regular grid over $\boldsymbol{\theta} = \{\tan^{-1} \alpha, \sigma_{\text{SHAM}}, \nu, x\}$, where we re-parametrise α via $\tan^{-1} \alpha$ to place it on a bounded interval. We note that this is an example of simulation-based inference (see e.g. Cranmer et al. 2020) as the likelihood function is not known analytically but rather built up from evaluations of the forward model (simulator).

We adopt separable, uniform priors on each parameter (Table 1):

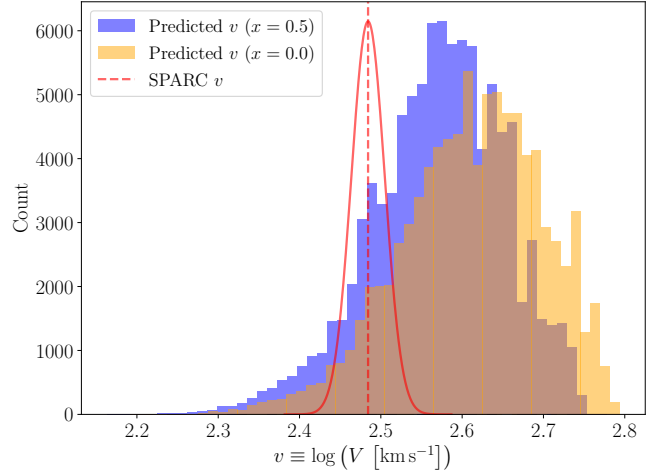


Figure 3. Illustration of the likelihood framework. Distribution of predicted $v \equiv \log V_{\max}$ for galaxy UGC02487 in the baseline model without halo selection ($\tan^{-1} \alpha = 0.0$, $\sigma_{\text{SHAM}} = 0.1$, $x = 0.0$, $\nu = -1.1$) in orange, and with added selection ($\tan^{-1} \alpha = 0.0$, $\sigma_{\text{SHAM}} = 0.1$, $x = 0.5$, $\nu = -1.1$) in blue, compared to its observed velocity and uncertainty (red). For this example, added selection results in a log-likelihood difference of $\Delta \ln \mathcal{L}(\mathcal{D}_i) \equiv \ln \mathcal{L}(\mathcal{D}_i \mid x = 0.5) - \ln \mathcal{L}(\mathcal{D}_i \mid x = 0) = 0.49$.

- $\tan^{-1} \alpha \sim \text{Uniform}(-\pi/2, \pi/2)$. This induces a Cauchy prior on α , $p(\alpha) \propto (1 + \alpha^2)^{-1}$, which is weakly informative in the tails while avoiding an arbitrary hard truncation in α -space. In practice we use a half-open interval $(-\pi/2 + \epsilon, \pi/2 - \epsilon)$ with a small ϵ that prevents the endpoints from mapping to $|\alpha| \rightarrow \infty$ due to floating-point precision.
- $\sigma_{\text{SHAM}} \sim \text{Uniform}(0.0, 1.0)$ dex. The upper limit is intentionally conservative relative to the $\sim 0.1\text{--}0.2$ dex values typically inferred in the literature, ensuring the prior is not informative over the physically relevant range.
- $\nu \sim \text{Uniform}(-3.0, 3.0)$. This covers a very broad range of halo response, from strong expansion to strong adiabatic contraction. Values $|\nu| \gtrsim 3$ often lead to unphysical or numerically unstable profiles and are disfavoured by existing constraints.
- $x \sim \text{Uniform}(0.01, 0.99)$. The lower limit avoids the degenerate case of $x = 0$ in our implementation, while the upper limit permits aggressive selection.

Between grid points, we interpolate the log-likelihood using multilinear interpolation. From Equation (17), the log-posterior is

$$\ln \mathcal{P}(\boldsymbol{\theta} \mid \mathcal{D}) = \ln \mathcal{L}(\mathcal{D} \mid \boldsymbol{\theta}) + \ln \pi(\boldsymbol{\theta}) + \text{const.}, \quad (23)$$

which we sample using an affine-invariant ensemble sampler algorithm implemented in `emcee` (Foreman-Mackey et al. 2013). Because the likelihood is computed via Monte Carlo averages, we maintain statistical consistency across $\boldsymbol{\theta}$ by ensuring the number of accepted draws per galaxy remains constant on average. Specifically, as the selection threshold x increases and the halo acceptance rate decreases, we scale N_{stellar} proportionally to keep the post-selection sample count stable.

To compare consistency of $(\alpha, \sigma_{\text{SHAM}})$ abundance matching parameters with the independent clustering constraints of S21, we compute the Bayes factor comparing the joint

Parameter	Description	Physical meaning	Prior
α	SHAM proxy	Exponent in the generalised halo proxy $m_\alpha \equiv M_{\text{vir}}(M_{\text{peak}}/M_{\text{vir}})^\alpha$ (see 3.1.1).	$\tan^{-1} \alpha \sim \text{Uniform}(-\pi/2, \pi/2)$
σ_{SHAM}	Intrinsic scatter	Log-normal scatter in M_\star at fixed halo proxy m_α , arising from stochastic galaxy formation processes.	$\text{Uniform}(0.0, 1.0)$ dex
ν	Halo response	Parameterises dark matter halo response to baryonic infall. $\nu = 0$: no change from NFW. $\nu > 0$: adiabatic contraction ($\nu = 1$ is fiducial). $\nu < 0$: halo expansion (e.g. from feedback-driven outflows).	$\text{Uniform}(-3.0, 3.0)$
x	Selection threshold	Galaxies are drawn only from haloes with $V_{\text{max,halo}}$ below the x^{th} percentile of the $V_{\text{max,halo}}$ distribution at fixed M_{vir} . Higher x implies stronger selection toward low-concentration haloes.	$\text{Uniform}(0.01, 0.99)$

Table 1. Model parameters, physical interpretation, and priors.

model (in which both datasets constrain the same underlying parameters) to independent models

$$K_{\text{joint}} = \frac{\mathcal{Z}_{\text{joint}}}{\mathcal{Z}_{\text{SPARC}} \mathcal{Z}_{\text{clustering}}}. \quad (24)$$

This is also interpreted on the Jeffreys scale, with values of $\log(K_{\text{joint}}) > 0$ indicating consistency and $\log(K_{\text{joint}}) < 0$ tension. Assuming flat priors, this simplifies to a function of the two independent posteriors $p(\boldsymbol{\theta})$ and the prior volume (V) with $K_{\text{joint}} = V \int p_{\text{SPARC}}(\boldsymbol{\theta}) p_{\text{clustering}}(\boldsymbol{\theta}) d\boldsymbol{\theta}$. As the problem is two-dimensional, we estimate posterior densities from samples using kernel density estimation. We apply a Jacobian transformation to reweight the posterior samples of S21 (which assumed a flat prior on α) to a common flat prior on $\tan^{-1} \alpha$.

3.3 Generating mock data

We draw independent mock datasets from the best-fitting parameter vector $\hat{\boldsymbol{\theta}}$ by re-running the full forward model and re-drawing all stochastic model elements (SHAM scatter, stellar/gas masses, halo-galaxy matching, and rotation curve computation). Because the selection step can reject a galaxy-halo pair in a given realisation, some galaxies may not be successfully matched to a halo. We handle this via rejection sampling: for each galaxy, we repeat the forward draw with independent random seeds until it is accepted by the selection, and retain the first accepted V_{max} . This yields one V_{max} per galaxy sampled from the model's conditional predictive distribution conditional on selection.

To emulate measurement noise, we perturb each simulated V_{max} using the fractional SPARC uncertainties. For the i^{th} galaxy, we set

$$\sigma_{V_{\text{max},i}} = V_{\text{max},i} \frac{\sigma_{V_{\text{max},i}}^{(\text{SPARC})}}{V_{\text{max},i}^{(\text{SPARC})}}, \quad (25)$$

and draw

$$V_{\text{max},i}^* \sim \mathcal{N}(V_{\text{max},i}, \sigma_{V_{\text{max},i}}^2). \quad (26)$$

4 RESULTS

We present posterior constraints from a baseline model without halo selection (Section 4.1), then introduce selection on $V_{\text{max,halo}}$ and compare model evidences (Section 4.2). Mock tests validating the inference pipeline are presented in Section A.

4.1 Model without selection

The left panel of Figure 4 shows the posterior constraints for the three-parameter model in which SPARC galaxies are assumed to be an unbiased draw from the full halo population ($\boldsymbol{\theta} = \{\tan^{-1} \alpha, \sigma_{\text{SHAM}}, \nu\}$). Three features emerge:

- Matching proxy: The posterior for $\tan^{-1} \alpha$ is prior-bound at the lower limit ($\tan^{-1} \alpha < -1.56$ at 2σ), implying $\alpha < -92.6$, i.e. a matching proxy that heavily suppresses satellite haloes.
- Scatter: The posterior peaks at $\sigma_{\text{SHAM}} = 0$ with a 1σ upper bound of ~ 0.2 dex, lower but consistent with the ~ 0.2 dex typically inferred for massive galaxies from clustering analyses (More et al. 2010; Reddick et al. 2013; Lehmann et al. 2016). (An extension to mass-dependent scatter is discussed in Section 5.1.)
- Halo response: The data favour expanded haloes, $\nu = -1.12^{+0.23}_{-0.22}$, corresponding to a reversal of the standard adiabatic contraction of comparable magnitude.

These values are in tension with independent clustering constraints, which favour $\alpha \gtrsim 0$ and $\sigma_{\text{SHAM}} \approx 0.2$ dex for massive galaxies (S21). SPARC targets H α -rich, late-type galaxies, which may not be representative of the full halo population at fixed stellar mass. To account for this, we introduce a halo-level selection on $V_{\text{max,halo}}$ at fixed M_{vir} (Section 3.1.4) and repeat the inference.

4.2 Model with selection

The right panel of Figure 4 shows the four-parameter posterior:

- Matching proxy: The constraint on α weakens substantially and shifts toward zero ($-0.8979 < \tan^{-1} \alpha < 0.3826$ at 68 per cent confidence), removing the tension with clustering constraints.
- Scatter: The preferred scatter increases to $\sigma_{\text{SHAM}} = 0.19^{+0.13}_{-0.11}$ dex, consistent with the ~ 0.2 dex for massive galaxies from clustering analyses (though also with zero scatter).
- Halo response: The posterior shifts to $\nu = 0.43^{+0.22}_{-0.24}$, indicating mild net contraction or no significant response.
- Selection: The selection parameter is tightly constrained to $x = 0.84 \pm 0.04$, meaning SPARC-like galaxies are drawn from the lowest ≈ 16 per cent of the $V_{\text{max,halo}}$ distribution at fixed M_{vir} .

Introducing selection thus removes the tension in α between

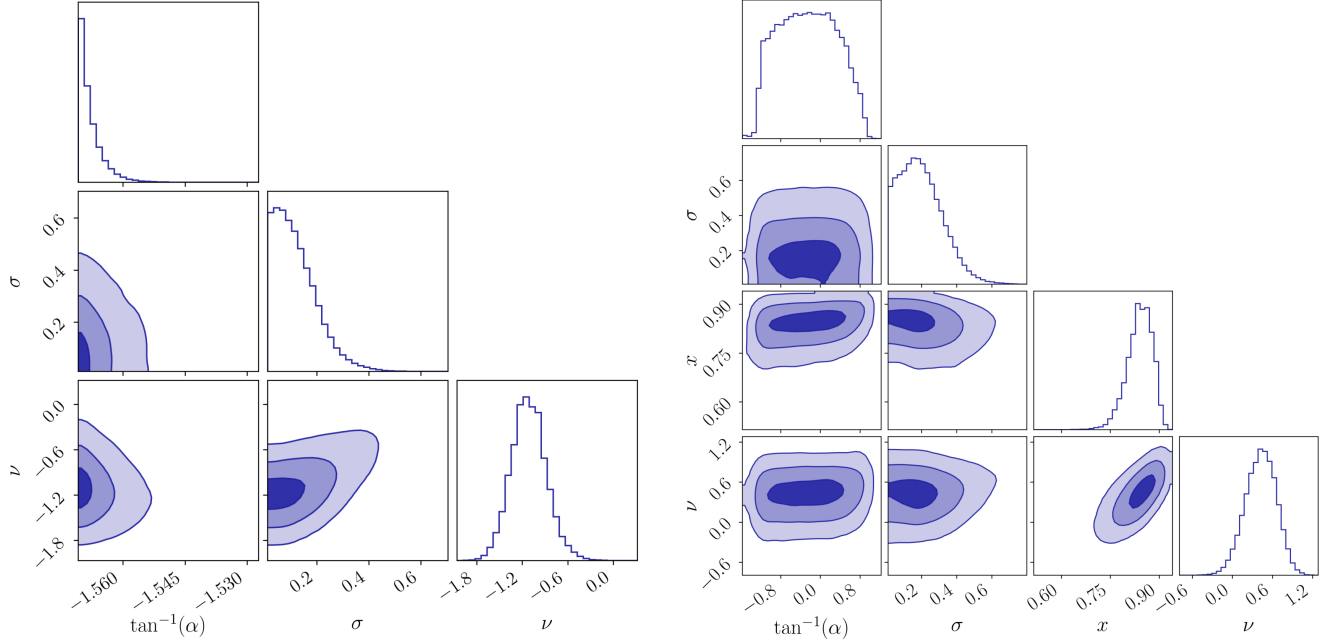


Figure 4. Posterior constraints on the three-parameter model (left) and the four-parameter model with selection on halo properties (right). Contours enclose 39.3, 86.5, and 98.9 per cent of posterior mass (corresponding to 1σ , 2σ , and 3σ for a 2D Gaussian). Without selection, the data favour extreme SHAM parameters in tension with independent constraints from galaxy clustering. Introducing selection brings all parameters into agreement with clustering, but requires a strong selection threshold ($x = 0.84 \pm 0.04$), meaning SPARC-like galaxies occupy the lowest ≈ 16 per cent of the $V_{\max, \text{halo}}$ distribution at fixed M_{vir} .

our work and clustering constraints, and shifts ν to values consistent with hydrodynamical simulations, but requires a very strong $V_{\max, \text{halo}}$ -based selection. Figure 6 compares the predicted BTFR from the baseline and selection models to the SPARC data: visually, both models successfully reproduce the tight correlation, slope, and scatter of the observed BTFR, but the selection model achieves this with parameters consistent with independent clustering constraints. (There may be a hint of curvature in the predicted relation in both cases, as was found to be a problem for the SPARC BTFR in [Desmond 2017](#).) The bottom left panel shows the distinct stellar-to-halo mass relations implied by the two models. While they converge at the high-mass end, they diverge at lower masses. The specific shape of the baseline relation is warped by the extreme α proxy required to match the observed BTFR in the absence of explicit selection. The bottom right panel shows the difference in log-likelihood $\Delta \ln \mathcal{L}$ between the two models for each individual galaxy as a function of baryonic mass. The selection model generally improves the fit at both the low-mass ($M_{\text{bar}} < 10^9 M_{\odot}$) and high-mass ($M_{\text{bar}} > 10^{11} M_{\odot}$) ends of the sample, likely due to decreased variance in the simulated V_{\max} distributions from the selection threshold. By truncating the halo population, the selection model eliminates the high-velocity tail (see Figure 3), narrowing the spread of predicted velocities for a given stellar mass and concentrating probability mass more tightly around the observed data.

Using the harmonic code ([Polanska et al. 2025](#)), we find $\Delta \ln \mathcal{Z} = 15.66$ and a Bayes factor of 6×10^6 in favour of the model that includes selection, indicating a decisive preference for including this additional parameter.

4.3 Comparison to clustering constraints

Figure 5 compares our posterior constraints on $(\alpha, \sigma_{\text{SHAM}})$ from the model including selection with those from the independent clustering analysis of [S21](#), which constrains the same SHAM parameters independently in four stellar mass bins. Specifically, we compare to their *optically-selected* sample constraints: our model assumes universal SHAM parameters for all galaxies, with H α -rich systems then selected based on halo properties, rather than treating H α -selected galaxies as a distinct population with their own AM parameters. We use their optically-selected sample with NSA Petrosian stellar masses for consistency with our stellar masses. We compute Bayes factors K_{joint} (Equation 24) to quantify the consistency between the two datasets. For the three highest mass bins ($\log(M_{\star}/M_{\odot}) > 10.7$), we find $\log K_{\text{joint}} = +0.36, -0.25$, and -0.38 respectively—all inconclusive or showing weak evidence for consistency on the Jeffreys scale. This indicates quantitatively that once halo selection is included, clustering and kinematics require consistent abundance-matching galaxy–halo connections at these masses. However, the lowest mass bin ($\log(M_{\star}/M_{\odot}) = 10.1\text{--}10.6$), which overlaps most closely with the SPARC sample, yields $\log K_{\text{joint}} = -1.07$, showing strong tension.

5 DISCUSSION

We interpret our results in the context of independent constraints and physical expectations (Section 5.1), discuss caveats and systematic uncertainties (Section 5.2), and outline directions for future work (Section 5.3).

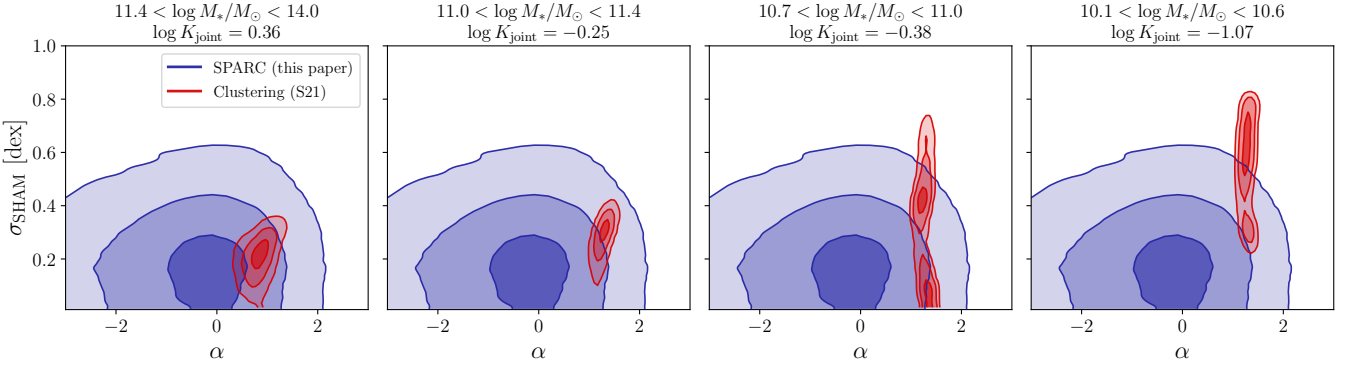


Figure 5. A comparison of the posterior constraints on the SHAM parameters from our SPARC analysis with selection (which assumes mass-independent SHAM parameters), with independent constraints from the clustering analysis of S21, for their four stellar mass bins (shown above the panels). All posteriors are reweighted to a common flat prior on $\tan^{-1} \alpha$. Contours enclose 39.3, 86.5, and 98.9 per cent of posterior mass (corresponding to 1σ , 2σ , and 3σ for a 2D Gaussian). The Bayes factor comparing the joint model (in which both datasets constrain the same underlying parameters) to independent models is shown above each panel, with the highest three stellar mass bins showing no more than weak evidence for tension, but the lowest mass bin (which is closest to the SPARC mean mass) indicating strong tension.

5.1 Interpretation and broader ramifications

A key innovation in our work is the development and use of a Bayesian forward model for constraining the galaxy–halo connection using kinematics that operates on a galaxy-by-galaxy level. By forward-modelling the data directly we can account for relevant effects in the direction in which they operate physically, and by making predictions for individual galaxies we ensure that the maximum amount of information in the data is utilised in the inference. This contrasts with methods that first summarise the data into scaling relations such as the TFR, which causes information loss.

The baseline three-parameter model (Section 4) yields extreme parameter values that, while reproducing the dynamics reasonably well, are difficult to reconcile with independent constraints. The inferred halo expansion ($\nu \approx -1$) reverses the standard adiabatic contraction by a comparable factor, consistent with previous AM-based analyses of the (stellar mass) TFR (Desmond & Wechsler 2015), which found that reproducing the observed normalisation requires weak contraction or net expansion. The SHAM scatter posterior peaks near zero, driven by the tight observed BTFR (~ 0.1 dex intrinsic scatter), though the constraint is broad and remains consistent at the 2σ level with the ~ 0.2 dex typically inferred for massive galaxies from galaxy clustering and satellite fractions (Reddick et al. 2013; Stiskalek et al. 2021). Most strikingly, the matching proxy parameter α is pinned to its prior bound, implying a prescription that heavily suppresses satellites at fixed stellar mass.

Physically, reduced star formation efficiency in satellite haloes is plausible: environmental processes such as ram-pressure stripping and strangulation can quench satellites, making them under-luminous relative to centrals of the same halo mass (Peng et al. 2010; Wetzel et al. 2013). However, the extreme α values preferred by the baseline model are in strong tension with clustering constraints, which favour $\alpha \gtrsim 0$ (S21). This tension suggests that the baseline model may be missing an important ingredient.

SPARC is not a representative optically-selected, stellar-mass-limited sample: it targets HI-rich, late-type galaxies

that may preferentially reside in less dense environments. Without accounting for selection effects, the model may absorb such population differences into α and ν , biasing both toward extreme values. In this interpretation, the baseline model compensates for unmodelled selection by (i) expanding haloes to lower V_{\max} at fixed baryonic mass, (ii) minimising SHAM scatter, and (iii) suppressing satellites that form stars efficiently. Introducing halo-level selection—expected a priori to some degree—largely resolves these tensions (Section 4). The matching proxy becomes consistent with $\alpha \gtrsim 0$, and the halo response shifts from strong expansion to mild contraction or no net response.

In Figure 5 we compared our posterior for the model with selection to those of S21 for the optically-selected sample. That analysis constrained AM parameters for HI-selected galaxies as we do here, using an HI-specific stellar mass function and treating HI-rich systems as a distinct population with their own SHAM parameters. Our approach differs conceptually: we assume all galaxies are populated according to a universal SHAM prescription, with survey-specific samples then arising from selection on halo properties. This avoids having to specify which fraction of the total simulated haloes appear in the HI survey before the abundance matching step, which is computationally expensive as it requires repeating abundance matching for each separate value of the selection parameter. Under this framework, the appropriate comparison is to optically-selected constraints, which should reflect the underlying universal relation we assume.

The best-fit selection parameter $x \approx 0.84$ indicates that SPARC-like galaxies occupy the lowest ~ 16 per cent of the $V_{\max, \text{halo}}$ distribution at fixed virial mass. Because $V_{\max, \text{halo}}$ at fixed M_{vir} correlates with concentration and formation time, this suggests that SPARC preferentially samples low-concentration, late-forming haloes. The general direction of this preference is physically plausible: gas-rich, actively star-forming disc galaxies are expected to reside in haloes that formed more recently and have shallower central potentials, allowing them to retain their cold gas reservoirs. This conclusion echoes Desmond & Wechsler (2015), who argued that selection effects preferentially eliminate fast-rotating galaxies

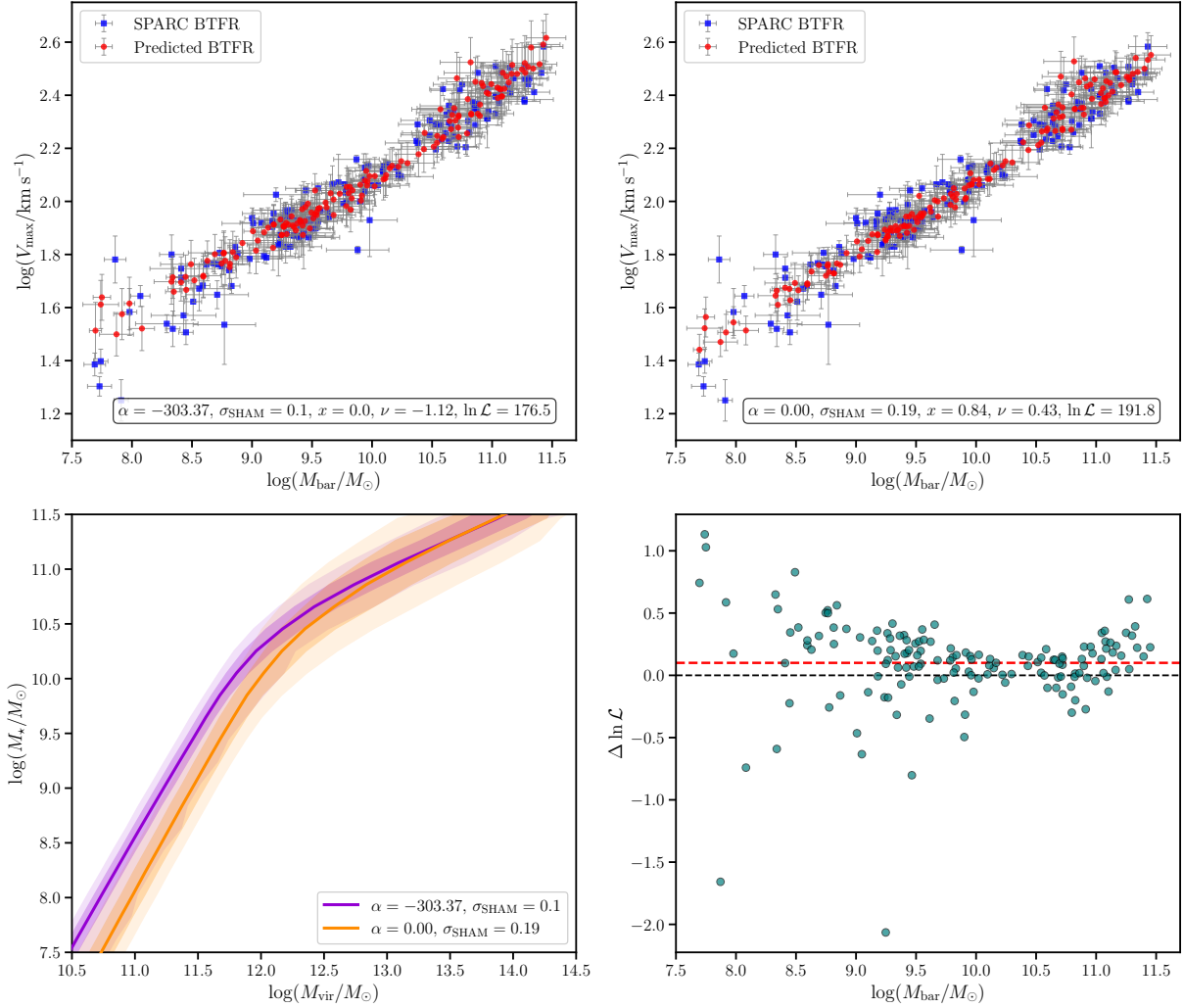


Figure 6. Comparison of the two best-fit models: the baseline 3-parameter model and the 4-parameter model with selection. **Top row:** BTFRs predicted by the two models overlaid on the observed SPARC data. **Bottom left:** The inferred stellar-to-halo mass relation for both models, showing the median, 1σ and 2σ credible intervals. **Bottom right:** The difference in log-likelihood per galaxy ($\Delta \ln \mathcal{L} = \ln \mathcal{L}_{\text{sel}} - \ln \mathcal{L}_{\text{base}}$) as a function of baryonic mass. Points above the dashed reference line favour the selection model. The red dashed line indicates the mean log-likelihood difference, $\ln \mathcal{L}_{\text{mean}} = 0.1$.

from kinematic samples, requiring late-type spirals to inhabit low-concentration haloes (around the lowest ~ 50 per cent) to match the observed BTFR normalisation. While they modelled this selection through the correlation between disc inclination and line-of-sight velocity, we parametrise it directly at the halo level; both approaches converge on the same physical picture.

Various studies have found differences in the properties of the haloes occupied by early and late-type galaxies. Wojtak & Mamon (2013) and Mandelbaum et al. (2016) find blue galaxies reside in lower concentration haloes at fixed halo mass, and the `UniverseMachine` model Behroozi et al. (2019) finds star-forming galaxies tend to live in haloes that are still accreting mass now. Both of these are qualitatively consistent with our V_{max} selection. However, these and other studies (Rodriguez-Puebla et al. 2015; Mandelbaum et al. 2016) have found blue and red galaxies occupy different SHMRs, whereas we assume a universal SHAM relation. In the future

our framework should be extended to allow different SHAM relations by galaxy-type, in addition to selection.

Both our study and Desmond & Wechsler (2015) require strong selection, with our tighter threshold (~ 16 vs ~ 50 per cent) likely reflecting a combination of the smaller, more targeted sample and more constraining per-galaxy likelihood framework employed here. Whether such a tight connection between halo properties and HI content exists in nature remains unknown. The $M_{\text{HI}}-M_{\star}$ relation exhibits substantial scatter (~ 0.3 – 0.4 dex; Rafrat 2021; Pan et al. 2025), suggesting that gas content is not tightly determined by stellar mass alone. It would therefore be surprising if $V_{\text{max,halo}}$ at fixed M_{vir} —or any other proxy of the halo mass distribution—could strongly predict HI content. One possibility is that the extreme selection parameter reflects a weaker underlying correlation: if $V_{\text{max,halo}}$ is only loosely related to the observables that actually drive SPARC selection, a strong threshold on $V_{\text{max,halo}}$ may be needed to approximate a more moderate selection on HI mass. Other possible candidates include whether

a galaxy is a central or a satellite and its merger history (both of which may predict the disruption of either the disc structure and/or the gas reservoir). Future analyses of samples with well-characterised selection functions in terms of H_I observables will be essential to assess whether halo-level selection can reconcile kinematic and clustering constraints in a physically realistic way.

An important issue is the potential mass-dependence of SHAM scatter. Our model assumes a single, mass-independent σ_{SHAM} , but the clustering analyses of S21 find that scatter varies significantly with stellar mass: they infer $\sigma_{\text{AM}} \approx 0.61_{-0.14}^{+0.11}$ dex for $10.1 < \log(M_{\star}/M_{\odot}) < 10.6$, decreasing to $\sigma_{\text{AM}} \approx 0.22_{-0.05}^{+0.05}$ dex for $11.4 < \log(M_{\star}/M_{\odot}) < 14.0$ for optically-selected samples. This creates a potential tension: SPARC predominantly samples lower-mass galaxies, where clustering predicts the largest SHAM scatter, yet the observed BTFR remains tight (~ 0.1 dex intrinsic scatter) across the full mass range. If the galaxy–halo connection truly has ~ 0.5 dex scatter at low masses, it is unclear how SPARC kinematics can be so well-behaved—selection alone cannot easily suppress scatter that is intrinsic to the SHAM relation. A binned analysis of SPARC galaxies in stellar mass could help disentangle these effects, though it would further complicate the selection modelling. Extending the framework to mass-dependent $\sigma_{\text{SHAM}}(M_{\star})$ will be necessary to fully assess whether kinematics and clustering can be jointly satisfied.

Relatedly, Macciò et al. (2020) tested AM predictions using dynamical masses for 190 Virgo cluster galaxies spanning $10^8 < M_{\star}/M_{\odot} < 10^{11}$, finding that observed scatter exceeds AM predictions by a factor of ~ 5 ; however, they argued this was dominated by measurement uncertainties, illustrating the difficulty of finding well-controlled kinematic samples for such tests. Other clustering-based studies have found no evidence for mass-dependent scatter in the galaxy–halo connection (e.g. Mitra & van den Bosch 2025, for haloes down to $10^{11.5} M_{\odot}$). Another possibility is a framework such as Modified Newtonian Dynamics (MOND; Milgrom 1983) which postulates a direct connection between baryons and dynamics and hence implies negligible scatter in the BTFR (for reviews see Famaey & McGaugh 2012; Banik & Zhao 2022; Famaey & Durakovic 2026; Desmond 2025).

Hydrodynamical simulations such as EAGLE (Schaller et al. 2015), Illustris/TNG (Genel et al. 2014; Pillepich et al. 2018), and FIRE (Hopkins et al. 2018) offer an alternative to the simple semi-empirical prescriptions employed here, producing direct predictions for galaxy dynamics. However, these simulations are calibrated on ensemble statistics (stellar mass functions, sizes, star formation rates) rather than individual galaxy kinematics. Recent work attempting to constrain hydrodynamical simulation parameters with observations has similarly relied on population-level properties such as the dark matter fraction as a function of stellar mass (Busillo et al. 2023, 2025), rather than per-galaxy velocity measurements. By employing simple semi-empirical constructions, we match the observed stellar and gas properties used as inputs to the forward model, allowing us to isolate which additional ingredients—such as halo response driven by baryonic feedback (e.g. Pontzen & Governato 2012) and sample selection—are required to reproduce the kinematic data, without relying on specific recipes for star formation and feedback. Hydrodynamical simulations also remain limited in volume and resolution, making it challenging to generate large mock samples

that match the observed stellar mass function while resolving internal kinematics (Jang et al. 2023). Our semi-empirical approach therefore provides a complementary method to extract information from galaxy kinematics and constrain the galaxy–halo connection, in which phenomenological ingredients can be investigated individually.

5.2 Caveats and systematics

Several simplifying assumptions underlie our model. First, we adopt a mass-independent SHAM prescription: the proxy parameter α and scatter σ_{SHAM} are constant across the stellar mass range probed by SPARC. As discussed in Section 5.1, clustering analyses find evidence for mass-dependent scatter, increasing toward lower masses (S21). If such trends are present, our single-valued parameters represent effective averages that may not accurately describe the edges of the mass distribution.

Second, our halo-level selection model is deliberately simple. The threshold parameter x imposes a sharp cut on $V_{\text{max,halo}}$ at fixed M_{vir} , effectively assuming a tight (deterministic) mapping between halo properties and H_I content. In reality, the connection between halo concentration, formation time, and cold gas mass is likely to have substantial scatter, modulated by environment, merger history, and stochastic feedback (Stiskalek et al. 2022). A more realistic treatment would introduce a probabilistic selection function with its own free parameters, at the cost of additional model complexity.

We assume an NFW density profile for all haloes, modified only by the global response parameter ν . A single-parameter halo response may be a strong simplification: hydrodynamical simulation studies have found the degree of contraction or expansion varies with radius, stellar-to-halo mass ratio, and assembly history in ways that a global ν cannot fully capture (Di Cintio et al. 2014; Tollet et al. 2016; Velmani & Paranjape 2023). We also assume spherical symmetry, whereas N -body simulations generically produce triaxial haloes; depending on the alignment of discs, triaxial haloes may lead to V_{max} variations of order ~ 10 per cent (Geha et al. 2006). These effects could introduce additional scatter or systematic shifts in the predicted rotation velocities.

We adopt the SPARC mass-to-light model, which assumes a fixed mass-to-light ratio in the $3.6 \mu\text{m}$ band for the bulge and disc. Spatially varying mass-to-light ratios—arising from radial gradients in stellar age, metallicity, or dust—could alter both the inferred total stellar mass and the shape of the stellar contribution to the rotation curve. Recent work using full stellar population synthesis modelling suggests that such variations do occur and can shift the inferred dark matter content (Vărăsteau et al. 2025). Fits to the Radial Acceleration Relation also prefer somewhat different mass-to-light ratios (Desmond et al. 2024). Systematic differences in M_{\star} would also propagate into our SHAM assignment and halo response inferences.

Finally, our dynamical model treats both the stellar and gas components as infinitesimally thin exponential discs with identical scale lengths. Real discs have finite vertical extent, which slightly reduces the mid-plane circular velocity at fixed mass and size. We also neglect pressure support: for gas-rich, low-mass systems the observed rotation velocity can underestimate the true circular velocity due to asymmetric drift,

and our model does not apply any such correction. Both effects are likely subdominant for the SPARC sample but could become more important for lower-mass or more dispersion-supported systems. For high-mass systems, a bigger concern is the simple treatment of bulges as spherical components; real bulges are often flattened or triaxial, which would alter their contribution to the rotation curve (Fisher & Drory 2008; Costantin et al. 2018; Desmond et al. 2024).

5.3 Future work

A natural next step is to apply this framework to samples with well-defined selection criteria. The MIGHTEE-H α survey (Maddox et al. 2021; Ponomareva et al. 2021) provides homogeneous photometry and kinematics for H α -selected galaxies, including linewidth measurements that serve as a proxy for V_{\max} whilst also extending such analyses to $z \sim 0.4$ (Jarvis et al. 2025). Applying our forward model to such samples would reduce systematic uncertainties associated with selection modelling and enable more robust inferences on the galaxy–halo connection. Wider field surveys such as ALFALFA (Haynes et al. 2018) could also be used, but at the expense of less precise photometry and auxiliary parameters such as inclination.

The selection model itself could be made more flexible. Rather than a sharp threshold on a single halo property, one could adopt probabilistic selection functions with scatter, or selection on multiple halo properties such as concentration or environment. Empirical relations between H α mass and stellar mass (Rafraf 2021) could inform such selection functions and help connect galaxy observables to halo properties.

Future H α surveys will dramatically expand the available samples. WALLABY on ASKAP (Koribalski & et al. 2020), MIGHTEE-H α on MeerKAT, and eventually the SKA (Blyth et al. 2015) will provide H α detections and linewidths for millions of galaxies extending to higher redshift. Applying our framework to these samples would enable evolutionary studies of the galaxy–halo connection and baryonic effects on halo structure across cosmic time.

The halo response model could be improved by adopting more physically-motivated prescriptions from hydrodynamical simulations. Di Cintio et al. (2014) and Tollet et al. (2016), for example, parameterise halo response as a function of stellar-to-halo mass ratio and predict both contraction and expansion depending on galaxy properties. More recent analytic models (Li et al. 2022) trace energy diffusion during gas ejection events and could provide a more physical basis for the response parameter. Incorporating such models would allow the halo response to depend on additional galaxy properties such as star-formation rate or gas fraction, rather than being a single global parameter.

Resolved rotation curve data contain yet more information—the Radial Acceleration Relation (e.g. McGaugh et al. 2016; Desmond 2017; Stiskalek & Desmond 2023; Desmond 2023; Desmond et al. 2024; Vărăsteau et al. 2025) demonstrates a tight correlation between observed and baryonic accelerations at each radius—and extending our framework to exploit this is a natural direction for future work. Another extension of this work is to the Milky Way satellite population, where forward-modelling pipelines have been used to constrain the galaxy–halo connection and satellite disruption from photometric census data (Nadler

et al. 2019, 2020), and semi-analytic frameworks provide physically-motivated ways to predict satellite properties from halo assembly histories (Kounkel et al. 2022; Kushwaha et al. 2024). Kinematics has begun to enter these analyses in compressed form, such as completeness-corrected velocity dispersion distributions, enabling constraints on small-scale dark matter physics (Kim et al. 2018; Kim & Peter 2021; Esteban et al. 2024). Our per-galaxy likelihood approach suggests a route to sharpen these constraints by forward-modelling the full line-of-sight velocity distributions of individual satellites within a similar Bayesian framework. This would leverage the full information content of stellar kinematics to probe dark matter structure and galaxy formation in the smallest haloes, and enable direct comparison to our study of predominantly isolated, late-type galaxies.

Finally, the likelihood framework could be adapted to constrain any model that predicts galaxy observables—such as hydrodynamical simulations or semi-empirical models like UNIVERSE MACHINE (Behroozi et al. 2019)—maximising the constraining power of these data compared to population-level summary statistics.

6 CONCLUSION

We present a Bayesian forward model for the maximum rotation velocities of SPARC galaxies, combining subhalo abundance matching with a parameterised halo response and constraining model parameters. Our likelihood is defined per galaxy, maximising constraining power by preventing information loss through compression of the data into summary statistics (e.g. the slope and intercept of the BTFR). Our conclusions are as follows:

- A baseline model without sample selection reproduces the observed V_{\max} distribution but requires extreme parameter values: strong halo expansion ($\nu = -1.12^{+0.23}_{-0.22}$), low SHAM scatter ($\sigma_{\text{SHAM}} < 0.15$ dex at 1σ ; a consequence of the BTFR’s low intrinsic scatter), and a SHAM proxy pinned to its lower prior bound ($\alpha < -92.6$), corresponding to the maximal suppression of stellar mass in stripped haloes possible within our SHAM parameterisation. This is in severe tension with independent clustering constraints (Figure 4), which favour $\alpha > 0.0$.
- Introducing halo-level selection on $V_{\max,\text{halo}}$ at fixed M_{vir} is decisively favoured (Bayes factor 6×10^6) and brings SHAM parameters into agreement with clustering: $\sigma_{\text{SHAM}} = 0.19^{+0.13}_{-0.11}$ dex and $\nu = 0.43^{+0.22}_{-0.24}$. The selection threshold $x = 0.84 \pm 0.04$ implies SPARC galaxies occupy the lowest ~ 16 per cent of $V_{\max,\text{halo}}$ at fixed M_{vir} (which correlates with preferential sampling of low-concentration, late-forming haloes).
- The inferred selection is extremely strong: given the large scatter in the $M_{\text{HI}}-M_{\star}$ relation, it is unclear whether $V_{\max,\text{halo}}$ can predict gas content precisely enough; alternatively, x may absorb model misspecification from unmodelled baryonic physics or non-standard dark matter phenomenology.
- Independent clustering constraints imply $\sigma_{\text{AM}} \sim 0.5$ dex at low stellar masses (S21), yet the BTFR remains tight across this range, suggesting residual tension. Extending the framework to mass-dependent scatter will be necessary to fully test

whether kinematics and clustering can be convincingly reconciled across the mass range in which they overlap.

Our analysis demonstrates the constraining power of resolved rotation curves on the galaxy–halo connection, and the importance of modelling sample selection when combining kinematic and clustering constraints. Forward-modelling frameworks of this type will be crucial for unlocking the full constraining power of upcoming $\text{H}\alpha$ surveys such as MIGHTEE, WALLABY and the SKA, which are set to provide linewidths for millions of galaxies to high redshift in the coming years. This will constrain halo structure, provide information on dark matter microphysics, test empirical models of the galaxy–halo connection and trace the co-evolution of baryonic and dark matter over cosmic time.

DATA AVAILABILITY

Data from the SPARC galaxy survey are publicly available at <http://astroweb.cwru.edu/SPARC/>, the Uchuu suite of N -body simulations at <https://skiesanduniverses.org/Simulations/Uchuu/>, and the NSA catalogue at <https://live-sdss4org-dr13.pantheonsite.io/>. All other data and computer code underlying this study will be made available upon reasonable request to the corresponding author.

APPENDIX A: MOCK TESTS

We validate the inference pipeline using 50 mock datasets generated from fiducial parameters ($\tan^{-1}\alpha = -0.5$, $\sigma_{\text{SHAM}}=0.1$, $x=0.5$, $\nu=0.789$) with observational noise added as per Equations (25) and (26). Each mock is analysed with the same priors and pipeline as the real data. Figure 7 shows posterior constraints for three realisations: the true parameter values (solid lines) lie within the 1σ credible regions in most cases. Across all 50 mocks, the distribution of posterior residuals relative to the injected values is consistent with the expected coverage, confirming that the pipeline is well-calibrated.

Comparing real and mock posteriors, the constraint on α is of similar width in both, σ_{SHAM} is slightly more constrained in the mocks and x is much more constrained in the real data than in the mocks. This discrepancy suggests there may be additional sources of systematic and/or statistical uncertainty present in the real data compared to the mocks.

ACKNOWLEDGEMENTS

We thank Anastasia Ponomareva, Andreea Varasteanu and Federico Lelli for useful inputs and discussion.

FB, TY and MJJ acknowledge support from UKRI Frontiers Research Grant [EP/X026639/1], which was selected by the ERC. FB also acknowledges support from the Oxford University Astrophysics Summer Research Programme. HD is supported by a Royal Society University Research Fellowship (grant no. 211046). RS acknowledges financial support from STFC Grant No. ST/X0508664/1 and the Snell Exhibition of Balliol College, Oxford.

We thank Jonathan Patterson for smoothly running the

Glamdring Cluster hosted by the University of Oxford, where the data processing was performed.

REFERENCES

Albareti F. D., et al., 2017, *ApJ Supplement Series*, 233, 25
 Banik I., Zhao H., 2022, *Symmetry*, 14, 1331
 Behroozi P. S., Conroy C., Wechsler R. H., 2010, *ApJ*, 717, 379
 Behroozi P. S., Wechsler R. H., Wu H.-Y., 2012a, *ApJ*, 762, 109
 Behroozi P. S., Wechsler R. H., Wu H.-Y., Busha M. T., Klypin A. A., Primack J. R., 2012b, *ApJ*, 763, 18
 Behroozi P., Wechsler R. H., Hearn A. P., Conroy C., 2019, *MNRAS*, 488, 3143
 Blumenthal G. R., Faber S. M., Flores R., Primack J. R., 1986, *ApJ*, 301, 27
 Blyth S., et al., 2015, in Advancing Astrophysics with the Square Kilometre Array (AASKA14). p. 128 ([arXiv:1501.01295](https://arxiv.org/abs/1501.01295)), doi:10.22323/1.215.0128
 Blyth S., et al., 2016, in MeerKAT Science: On the Pathway to the SKA. p. 4, doi:10.22323/1.277.0004
 Bosma A., 1981, *The Astronomical Journal*, 86, 1825
 Bryan G. L., Norman M. L., 1998, *ApJ*, 495, 80
 Busillo V., Tortora C., Napolitano N. R., Koopmans L. V. E., Covone G., Gentile F., Hunt. L. K., 2023, *MNRAS*, 525, 6191
 Busillo V., Tortora C., Covone G., Koopmans L. V. E., Silvestrini M., Napolitano N. R., 2025, *A&A*, 693, A112
 Conroy C., Wechsler R. H., Kravtsov A. V., 2006, *ApJ*, 647, 201
 Costantin L., Méndez-Abreu J., Corsini E. M., Morelli L., Dalla Bontà E., Pizzella A., 2018, *Monthly Notices of the Royal Astronomical Society*, 481, 3623
 Cranmer K., Brehmer J., Louppe G., 2020, *Proc. Natl. Acad. Sci.*, 117, 30055
 Desmond H., 2017, *MNRAS*, 472, L35
 Desmond H., 2023, *MNRAS*, 526, 3342
 Desmond H., 2025, [arXiv e-prints](https://arxiv.org/abs/2505.21638), p. arXiv:2505.21638
 Desmond H., Wechsler R. H., 2015, *MNRAS*, 454, 322
 Desmond H., Katz H., Lelli F., McGaugh S., 2019, *MNRAS*, 484, 239
 Desmond H., Hees A., Famaey B., 2024, *MNRAS*, 530, 1781
 Di Cintio A., Brook C. B., Macciò A. V., Stinson G. S., Knebe A., Dutton A. A., Wadsley J., 2014, *MNRAS*, 437, 415
 Dutton A. A., van den Bosch F. C., Dekel A., Courteau S., 2007, *ApJ*, 654, 27
 Esteban I., Peter A. H. G., Kim S. Y., 2024, *Phys. Rev. D*, 110, 123013
 Famaey B., Durakovic A., 2026, in Encyclopedia of Astrophysics, Volume 5. pp 121–142 ([arXiv:2501.17006](https://arxiv.org/abs/2501.17006)), doi:10.1016/B978-0-443-21439-4.00081-X
 Famaey B., McGaugh S. S., 2012, *Living Reviews in Relativity*, 15, 10
 Ferrero I., et al., 2017, *MNRAS*, 464, 4736
 Fisher D. B., Drory N., 2008, *Astronomical Journal*, 136, 773
 Foreman-Mackey D., Hogg D. W., Lang D., Goodman J., 2013, *Publications of the Astronomical Society of the Pacific*, 125, 306–312
 Geha M., Blanton M. R., Masjedi M., West A. A., 2006, *ApJ*, 653, 240
 Genel S., et al., 2014, *MNRAS*, 445, 175
 Gnedin O. Y., Ceverino D., Gnedin N. Y., Klypin A. A., Kravtsov A. V., Levine R., Nagai D., Yepes G., 2011, [arXiv e-prints](https://arxiv.org/abs/1108.5736), p. arXiv:1108.5736
 Haynes M. P., et al., 2018, *ApJ*, 861, 49
 Hearn A. P., Watson D. F., 2013, *MNRAS*, 435, 1313
 Hopkins P. F., et al., 2018, *MNRAS*, 480, 800
 Ishiyama T., Fukushige T., Makino J., 2009, *PASJ*, 61, 1319
 Ishiyama T., Nitadori K., Makino J., 2012, in SC’12: Proceedings of

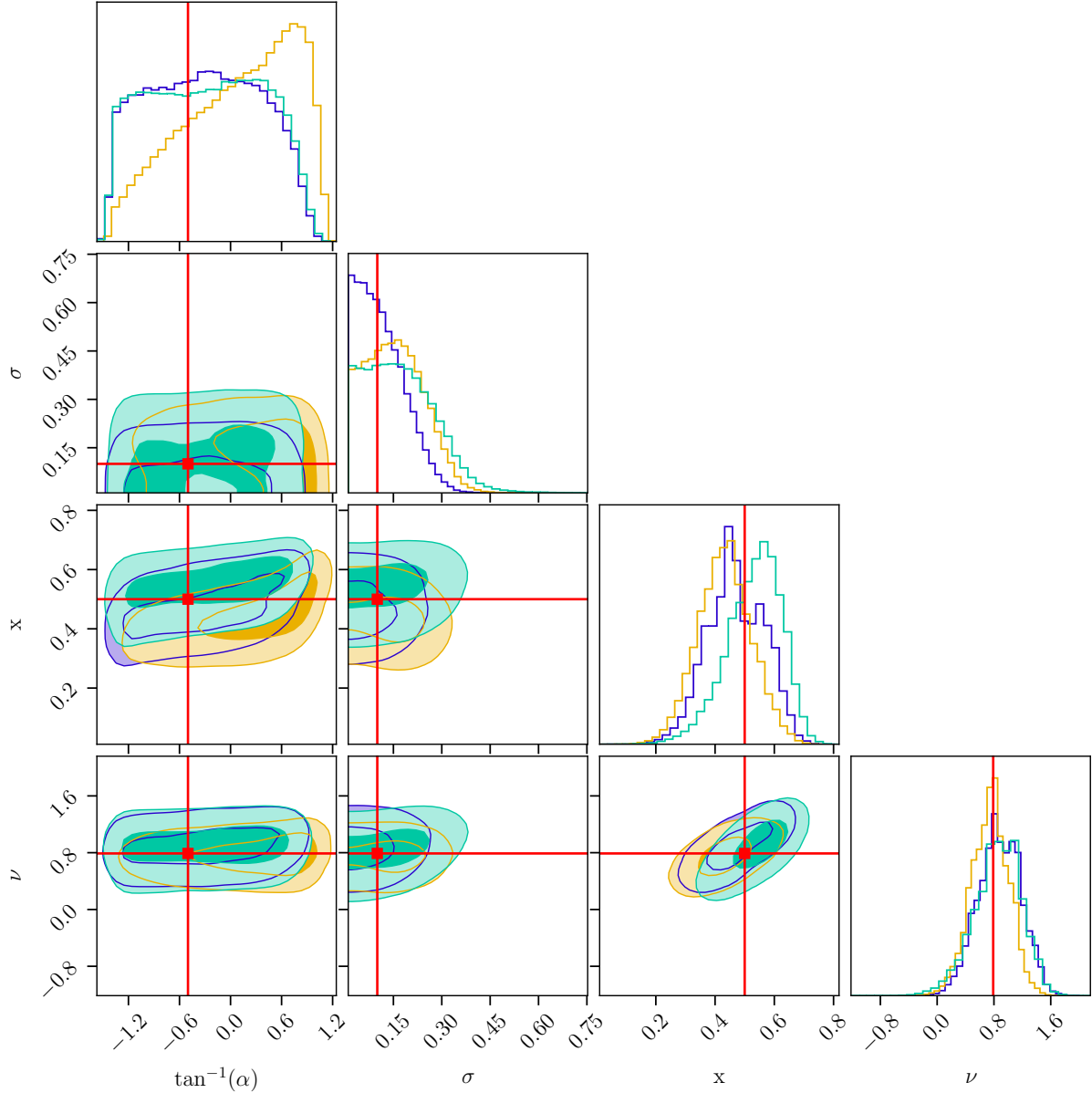


Figure 7. Mock validation of the inference pipeline. Contours enclose 39.3 and 86.5 per cent of the 2D posterior (1 σ and 2 σ for a 2D Gaussian). We show constraints for three independent mock datasets generated at $\theta_{\text{true}} = (\tan^{-1} \alpha, \sigma_{\text{SHAM}}, x, \nu) = (-0.5, 0.1, 0.5, 0.789)$. The red lines indicate these truths. The true parameters fall within the 1 σ contours in most panels, demonstrating that the pipeline produces well-calibrated posteriors.

the International Conference on High Performance Computing, Networking, Storage and Analysis. pp 1–10

Ishiyama T., et al., 2021, [MNRAS](#), 506, 4210

Jang K. M., Chen J., Kang Y., Kim J., Lee J., Duarte F., 2023, [arXiv e-prints](#), p. [arXiv:2306.04662](#)

Jarvis M., et al., 2016, in MeerKAT Science: On the Pathway to the SKA. p. 6 ([arXiv:1709.01901](#)), doi:10.22323/1.277.0006

Jarvis M. J., et al., 2025, [MNRAS](#), 544, 193

Jeffreys H., 1939, Theory of Probability. Oxford, England

Kim S. Y., Peter A. H. G., 2021, [arXiv e-prints](#), p. [arXiv:2106.09050](#)

Kim S. Y., Peter A. H. G., Hargis J. R., 2018, [Phys. Rev. Lett.](#), 121, 211302

Koribalski B. S., et al. 2020, [Astrophysics and Space Science](#), 365, 118

Kounkel M., Stassun K. G., Covey K., Hartmann L., 2022, [MNRAS](#), 517, 161

Kravtsov A. V., Berlind A. A., Wechsler R. H., Klypin A. A., Gottlöber S., Allgood B., Primack J. R., 2004a, [ApJ](#), 609, 35

Kravtsov A. V., Gnedin O. Y., Klypin A. A., 2004b, [The Astrophysical Journal](#), 609, 482

Kushwaha A., Malik S., Shankaranarayanan S., 2024, [MNRAS](#), 527, 4378

Lehmann B. V., Mao Y.-Y., Becker M. R., Skillman S. W., Wechsler R. H., 2016, [ApJ](#), 834, 37

Lelli F., McGaugh S. S., Schombert J. M., 2016, [AJ](#), 152, 157

Lelli F., McGaugh S. S., Schombert J. M., Desmond H., Katz H., 2019, [MNRAS](#), 484, 3267

Li Z., Dekel A., Mandelker N., Freundlich J., François T. L., 2022, [Monthly Notices of the Royal Astronomical Society](#), 518, 5356

Macchiò A. V., Courteau S., Ouellette N. N.-Q., Dutton A. A., 2020, *MNRAS*, **496**, L101

Maddox N., et al., 2021, *A&A*, **646**, A35

Mandelbaum R., Wang W., Zu Y., White S., Henriques B., More S., 2016, *Monthly Notices of the Royal Astronomical Society*, **457**, 3200

Mao Y.-Y., Zentner A. R., Wechsler R. H., 2017, *Monthly Notices of the Royal Astronomical Society*, **474**, 5143

Martin D. C., et al., 2005, *ApJ*, **619**, L1

McGaugh S. S., Schombert J. M., 2014, *AJ*, **148**, 77

McGaugh S. S., Schombert J. M., Bothun G. D., de Blok W. J. G., 2000, *ApJ*, **533**, L99

McGaugh S. S., Lelli F., Schombert J. M., 2016, *Phys. Rev. Lett.*, **117**, 201101

Milgrom M., 1983, *ApJ*, **270**, 365

Mitra K., van den Bosch F. C., 2025, *arXiv e-prints*, p. arXiv:2510.08421

More S., van den Bosch F. C., Cacciato M., Skibba R., Mo H. J., Yang X., 2010, *Monthly Notices of the Royal Astronomical Society*, **410**, 210–226

Moster B. P., Somerville R. S., Maulbetsch C., van den Bosch F. C., Macchiò A. V., Naab T., Oser L., 2010, *ApJ*, **710**, 903

Nadler E. O., Mao Y.-Y., Green G. M., Wechsler R. H., 2019, *ApJ*, **873**, 34

Nadler E. O., et al., 2020, *ApJ*, **893**, 48

Navarro J. F., Frenk C. S., White S. D. M., 1997, *ApJ*, **490**, 493

Pan H., et al., 2025, *MNRAS*, **544**, 1710

Peng Y.-j., et al., 2010, *ApJ*, **721**, 193

Pillepich A., et al., 2018, *MNRAS*, **473**, 4077

Planck Collaboration et al., 2020, *A&A*, **641**, A6

Polanska A., Price M. A., Piras D., Spurio Mancini A., McEwen J. D., 2025, *The Open Journal of Astrophysics*, **8**, 156

Ponomareva A. A., Verheijen M. A. W., Peletier R. F., Bosma A., 2017, *MNRAS*, **469**, 2387

Ponomareva A. A., Verheijen M. A. W., Papastergis E., Bosma A., Peletier R. F., 2018, *MNRAS*, **474**, 4366

Ponomareva A. A., et al., 2021, *MNRAS*, **508**, 1195

Pontzen A., Governato F., 2012, *MNRAS*, **421**, 3464

Rafraf H., 2021, *arXiv e-prints*, p. arXiv:2108.10449

Reddick R. M., Wechsler R. H., Tinker J. L., Behroozi P. S., 2013, *ApJ*, **771**, 30

Rhee J., et al., 2023, *MNRAS*, **518**, 4646

Rodriguez-Puebla A., Avila-Reese V., Yang X., Foucaud S., Drory N., Jing Y. P., 2015, *The Astrophysical Journal*, **799**, 130

Rubin V. C., Ford W. Kent J., 1970, *The Astrophysical Journal*, **159**, 379

Schaller M., Dalla Vecchia C., Schaye J., Bower R. G., Theuns T., Crain R. A., Furlong M., McCarthy I. G., 2015, *MNRAS*, **454**, 2277

Schaye J., et al., 2015, *MNRAS*, **446**, 521

Schmidt M., 1968, *ApJ*, **151**, 393

Sofue Y., Rubin V., 2001, *ARA&A*, **39**, 137

Stiskalek R., Desmond H., 2023, *MNRAS*, **525**, 6130

Stiskalek R., Desmond H., Holvey T., Jones M. G., 2021, *MNRAS*, **506**, 3205

Stiskalek R., Bartlett D. J., Desmond H., Anbajagane D., 2022, *MNRAS*, **514**, 4026

Tasitsiomi A., Kravtsov A. V., Wechsler R. H., Primack J. R., 2004, *ApJ*, **614**, 533

Tinker J. L., et al., 2017, *ApJ*, **839**, 121

Tollet E., et al., 2016, *MNRAS*, **456**, 3542

Trujillo-Gomez S., Klypin A., Primack J., Romanowsky A. J., 2011, *ApJ*, **742**, 16

Tully R. B., Fisher J. R., 1977, *Astronomy and Astrophysics*, **54**, 661

Vale A., Ostriker J. P., 2004, *MNRAS*, **353**, 189

Vale A., Ostriker J. P., 2006, *MNRAS*, **371**, 1173

Velmani P., Paranjape A., 2023, *MNRAS*, **520**, 2867

Vărășteanu A. A., et al., 2025, *MNRAS*, **541**, 2366

Wechsler R. H., Tinker J. L., 2018, *ARA&A*, **56**, 435

Werner M. W., et al., 2004, *ApJS*, **154**, 1

Wetzel A. R., Tinker J. L., Conroy C., van den Bosch F. C., 2013, *MNRAS*, **432**, 336

Wojtak R., Mamon G. A., 2013, *MNRAS*, **428**, 2407

Yasin T., Desmond H., Devriendt J., Slyz A., 2023a, *MNRAS*, **525**, 5066

Yasin T., Desmond H., Devriendt J., Slyz A., 2023b, *MNRAS*, **526**, 5861

Zentner A. R., Hearin A. P., van den Bosch F. C., 2014, *MNRAS*, **443**, 3044

This paper has been typeset from a *T_EX/L_AT_EX* file prepared by the author.